Delft University of Technology

Power Disequilibrium Suppression in Bipolar DC Distribution Grids By Using A Series-Parallel Power Flow Controller

Liao, Jianquan; Zhou, Niancheng; Qin, Zian; Wang, Qianggang; Bauer, Pavol

DOI
10.1109/TPWRD.2022.3180839

Publication date
2023

Document Version
Final published version

Published in
IEEE Transactions on Power Delivery

Citation (APA)
Liao, J., Zhou, N., Qin, Z., Wang, Q., & Bauer, P. (2023). Power Disequilibrium Suppression in Bipolar DC Distribution Grids By Using A Series-Parallel Power Flow Controller. *IEEE Transactions on Power Delivery*, *38*(1), 117 - 132. Article 9789728. https://doi.org/10.1109/TPWRD.2022.3180839

Power Disequilibrium Suppression in Bipolar DC Distribution Grids by Using a Series-Parallel Power Flow Controller

Jianquan Liao, *Member, IEEE*, Niancheng Zhou, *Member, IEEE*, Zian Qin, *Senior Member, IEEE*,
Qianggang Wang, *Member, IEEE*, and Pavol Bauer, *Senior Member, IEEE*

***Abstract*—The unbalanced power between positive and negative poles in a bipolar DC distribution network (DC-DN) generates an unbalanced current at the neutral line, which enlarges the power losses of the system and the voltage deviation of DC loads. An unbalanced power suppression strategy based on a series-parallel power flow controller (SP-PFC) is proposed in this paper. The SP-PFC is adopted as the interconnection between two different DC-DNs. The topology and operating modes of SP-PFC are analyzed. Subsequently, SP-PFC output voltage and line current expressions under constant power control are derived. The nonlinear relationship between the output voltage and line current is linearized at the operating point. On this basis, the influences of unbalanced load and receiving-end voltage on the SP-PFC are investigated. A small-signal model of bipolar DC-DN containing an SP-PFC is established, and the system stability is analyzed. A simulation model of the bipolar DC distribution network containing an SP-PFC is built up in MATLAB/Simulink, and the effectiveness of the SP-PFC in the suppression of unbalanced power is verified.**

***Index Terms*—Bipolar DC distribution network, unbalanced power, power flow controller, constant power control.**

NOMENCLATURE

S	Switches of SP-PFC
T_1	Isolation transformer
L_σ	The leakage reactance of T_1
R_L	The DC line equivalent resistance
N_i	Node i ($i = 12,3$)
$V_{i\mathrm{p,n}}$	Positive (p) and negative(n) pole voltage of node i
$V_\mathrm{Lp,n}, (V_\mathrm{L})$	Positive and negative line-side voltage
$I_\mathrm{Lp}, I_\mathrm{nu}, I_\mathrm{Ln}$	Positive pole, neutral line, negative pole currents
$I_\mathrm{sp,n}$	Positive and negative voltage source current
P_i1	Primary-side power of positive SP-PFC
P_i2	Primary -side power of negative SP-PFC
P_o1	Secondary -side power of positive SP-PFC
P_o2	Secondary-side power of negative SP-PFC
$V_\mathrm{dp,n}, (V_\mathrm{dc})$	Secondary-side voltage of DAB
$I_\mathrm{kp,n}$	Primary-side current of SP-PFC
$V_\mathrm{kp,n}$	Output voltage of SP-PFC
$\eta_\mathrm{p,n}$	Efficiency of SP-PFC
$P_\mathrm{Lp,n}$	Power transmitted by the positive and negative poles
P	Reference power of transmission line
V_0, I_0	Rated voltage and current
R_c	Equivalent internal resistance of SP-PFC
$R_\mathrm{p,n}$	Equivalent resistances of local positive and negative DC loads
C_1, C_2	Filter capacitances of FBC
L_1, L_2	Filter inductances of FBC
$i_\mathrm{L1}, i_\mathrm{L2}$	Inductance current of FBC
$v_\mathrm{kp}, v_\mathrm{kn}$	Instantaneous values of V_kp and V_kn
$i_\mathrm{Lp}, i_\mathrm{nu}, i_\mathrm{Ln}$	Instantaneous values of I_Lp, I_nu, I_Ln
$d_\mathrm{p}, d_\mathrm{n}$	Duty cycles of positive and negative poles of FBC
$K_\mathrm{p}, K_\mathrm{i}$	Proportionality and integral coefficients
$P^*{}_\mathrm{t}$	Reference values of DC transmission power

Manuscript received 31 October 2021; revised 3 February 2022 and 13 April 2022; accepted 30 May 2022. Date of publication 7 June 2022; date of current version 24 January 2023. This work was supported by the National Natural Science Foundation of China under Grants 51877017 and 52077017. Paper no. TPWRD-01635-2021. *(Corresponding author: Zian Qin.)*

Jianquan Liao is with the School of Electrical Engineering at Sichuan University, Chengdu 610065, China (e-mail: jquanliao@scu.edu.cn).

Niancheng Zhou and Qianggang Wang are with the State Key Laboratory of Power Transmission Equipment and System Security and New Technology, Chongqing University, Chongqing 400044, China (e-mail: cee_nczhou@cqu.edu.cn; yitagou@qq.com).

Zian Qin and Pavol Bauer are with the Department of Electrical Sustainable Energy, DCE&S group, TU Delft, 2628 CD Delft, The Netherlands (e-mail: z.qin-2@tudelft.nl; p.bauer@tudelft.nl).

Color versions of one or more figures in this article are available at https://doi.org/10.1109/TPWRD.2022.3180839.

Digital Object Identifier 10.1109/TPWRD.2022.3180839

V^*_{k}	Reference values of V_{kp} and V_{kn}
$U_{\mathrm{cp,n}}$	Voltage of current flow controller
$C_{\mathrm{fp,n}}$	Capacitor of current flow controller
$G_{\mathrm{pp}}(\mathrm{s})$, $G_{\mathrm{nn}}(s)$, $G_{\mathrm{pn}}(\mathrm{s})$, $G_{\mathrm{np}}(s)$	Transfer function of d_{p}, d_{n} to v_{kp} and v_{kn}
I_{set}	Current Threshold for Bypass Control
$I_{\mathrm{nu,s}}$	Neutral current on the left side of the SP-PFC

I. INTRODUCTION

THE proportion and capacity of distributed generations (DGs) such as photovoltaic power and wind power are continuously increasing in recent years. Besides, DC loads such as electric vehicles, data centers, and LED lights are becoming more and more common. The “DC feature” of the current power distribution networks is becoming increasingly prominent [1], [2]. Receiving large-scale DGs and DC loads via AC distribution networks (AC-DNs) adds the conversion link and leads to problems regarding frequency stabilization and reactive power compensation, etc. [3]. Compared with AC-DNs, DC distribution networks (DC-DNs) have higher power quality, higher power supply reliability, and larger power supply capacity [1]–[3]. However, the structure of DC-DNs is becoming more and more complicated, and the regulation of power flow (PF) cannot be fully controlled through the DC convertor station [4]. In some cases, this may cause line overload and threaten the safe and efficient operation of the system [5].

To tackle this problem, many scholars have introduced a power flow controller (PFC) into DC-DNs [6]. According to the connection mode to DC-DNs, PFC can be divided into 1) series type (S-PFC), parallel type (P-PFC) and series-parallel type (SP-PFC) [7], where the typical representatives of S-PFC include variable resistance-type PFC (VR-PFC) and inter-line PFC (IL-PFC). The equivalent resistance of VR-PFC can be changed flexibly through switching. Therefore, the PF can be regulated flexibly [8], [9]. The principle and control of VR-PFC are simple. However, it consumes massive power, which degrades the system operating efficiency. IL-PFC controls PF through the energy exchange between different DC lines [10]–[13]. Under regular operation, IL-PFC regulates the PF through the time-sharing series connection of one capacitor into two separate DC lines. IL-PFC has the advantage of simple structure and low cost, but it will introduce current ripples [7]. Paralleled PFC is essentially a DC transformer, which needs to withstand the rated power of DC-DNs [14]. Therefore, the initial investment of this PFC is high, which does not apply to PF regulation in DC-DNs.

In [15]–[17], the topology of series-parallel PFC (SP-PFC) is proposed. The input of SP-PFC is in parallel with the DC bus, and its output is in series with the DC transmission line. The primary and secondary sides of this PFC are connected through an isolation transformer. Therefore, this PFC only needs to process the partial power of DC-DNs, which has a considerable cost advantage. In addition, this PFC can realize PF control without relying on the power exchange between different DC lines. In [16], the fault protection method of a DC-DN containing SP-PFC is developed. The DC fault is cleared through a solid-state DC circuit breaker (DCCB), and the SP-PFC can be bypassed quickly from the DC fault. However, the PF control performance of SP-PFC is not analyzed. In [17], the application of SP-PFC in bipolar DC-DNs is investigated. However, only the characteristics of SP-PFC are analyzed. The characteristics of bipolar DC-DNs under unbalanced conditions are not mentioned.

Compared with unipolar DC-DNs, bipolar DC-DNs have a multi-voltage interface, which can satisfy the diversified demands of customers. In addition, bipolar DC-DNs have the advantages of lower power losses, lower construction costs, and higher reliability than unipolar DC-DNs [18], [19]. However, the PF control of bipolar DC-DNs is more complicated than unipolar due to unbalanced power between positive and negative poles. When the DC load or the receiving-end voltage is unbalanced, the unbalanced current will be generated in the neutral line. This current will enlarge the power losses of the network and the deviation of node voltage.

Existing studies suppress the unbalanced current of bipolar DC-DNs from the source side and the load side. In [19], a DC electric spring (DC-ES) based unbalanced voltage suppression method is investigated. The positive and negative pole voltage is found to be coupled when the DC loads are unbalanced. Therefore, decoupling control is proposed to improve the dynamic performance of DC-ES. However, the performance of unbalanced voltage suppression is influenced by the power of the non-critical load. In [20], an unbalanced current (voltage) suppression method based on a voltage balancer (VB) is proposed. The VB is installed at the exit of the AC/DC converter. When the DC transmission line is long, the voltage drop of DC lines is significant. Therefore, the voltage quality of the end nodes cannot be guaranteed.

The methods mentioned above only ensure the balanced state of local loads but do not consider the system imbalance. In [21], the unbalanced DC loads in positive and negative poles are reconfigured online through the load-commutation switch, and the unbalanced current is mitigated significantly. However, this method needs lots of current and voltage sensors, communications, and switches. Therefore, the initial investment is high. In [22], a voltage regulation method is proposed based on the neutral to line drop compensation (NLDC) method. The unbalanced current and line impedance are considered to compensate for the neutral line potential fluctuation and voltage drop on the DC lines. Finally, the sending-end voltage is regulated through the droop control of the AC/DC converter. However, this method can only deal with minor unbalance conditions. Besides, only the droop control of the AC/DC converter is mentioned.

According to the above analysis, the unbalanced voltage can be suppressed using the PFC installed in the DC-DNs. By designing an appropriate PFC control scheme, it is possible to suppress unbalanced voltage while adjusting PF. This does not increase the construction cost of the bipolar DC-DNs, but also expands the function of the PFC.

The contributions of this paper are summarized as follows:

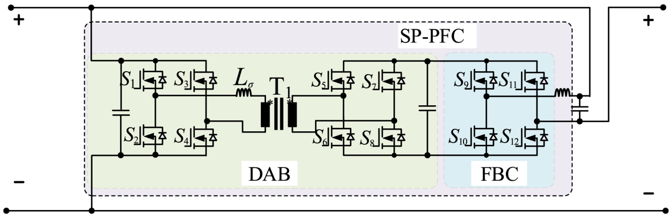

Fig. 1. The topology of the series-parallel power flow controller.

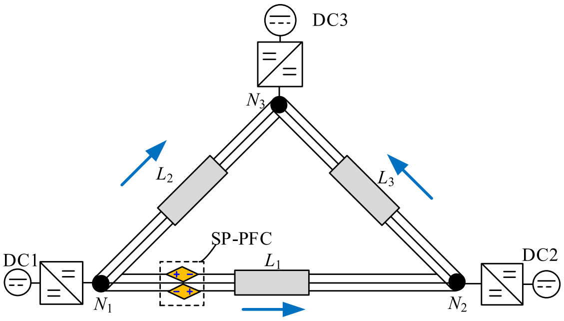

Fig. 2. A three-terminal ring bipolar DC-DN containing SP-PFC.

1) This paper proposes an SP-PFC-based unbalanced power suppression method. By installing an SP-PFC at the outlet of the sending-end node, the PF in positive and negative lines can be controlled flexibly.
2) the relationship between the output voltage of SP-PFC and line currents is analyzed. Besides, the control method and the operating mode of SP-PFC are introduced, which helps understand the characteristic of SP-PFC.
3) The influence of unbalanced receiving-end voltage and local loads are analyzed. With SP-PFC, the unbalanced current will be suppressed significantly. A small-signal model of bipolar DC-DN containing SP-PFC is established, and the transfer function between controlled quantity and output quantity is derived.

The rest of the paper is organized as follows: Section II introduces the topology and operating mode of SP-PFC, and the influence of unbalanced receiving-end voltage and DC load is analyzed; Section III analyzes the stability of bipolar DC-DNs containing SP-PFC; Section IV verifies the proposed method by using a bipolar DC-DNs simulation model in MATLAB/Simulink; and Section V concludes the paper.

II. UNBALANCED POWER FLOW ANALYSIS OF BIPOLAR DC-DNS

A. *The Topology and Operating Mode of SP-PFC*

The topology of the SP-PFC is shown in Fig. 1. Here, S_1-S_{12} represent switches of SP-PFC. SP-PFC consists of a dual active bridge (DAB) and a full-bridge converter (FBC). The primary side of DAB is in parallel connection to the DC bus, and the secondary side is connected with FBC. FBC is in a series connection to the DC transmission line. Because T_1 has a high transformation ratio and high switching frequency, its loss and volume are relatively small [16]. Besides, the primary side of SP-PFC has the characteristics of rated voltage and partial current, and the secondary side has the characteristics of partial voltage and rated current. Therefore, this SP-PFC only needs to process the partial power of the system [16], [23].

The operation modes of SP-PFC are summarized as follows. 1) Buck mode: Buck mode: DAB takes power from the DC bus, and FBC controls the output voltage of SP-PFC. 2) Unfolder mode: The output voltage of SP-PFC is controlled by DAB, while FBC controls the polarity of the output voltage. 3) Bypass mode: When the output voltage of SP-PFC exceeds the threshold, the SP-PFC will be bypassed. 4) Block mode: All the switches in FBC are blocked. Under this circumstance, the power on the secondary side of DAB will be fed back to the primary side.

According to the functions of DAB and FBC, the generic functionalities of SP-PFC are summarized as follows:

1) Voltage control: The phase shift control is applied to DAB, making it take power from the DC bus and output a stable voltage [14], [16]. For FBC, by monitoring the line voltage and adding it to the control feedback loop, SP-PFC can achieve flexible control of the line-side voltage [23].
2) Power control. If the current and voltage of the line can be monitored in real-time, the power delivered by the line can be used as the feedback input for the control. Therefore, the transmitted power of the line can be taken as the control objective. This function is beneficial for keeping the power exchange between two DC-DNs constants.
3) Fault current limiting. In [24], a coordination strategy between SP-PFC and hybrid DCCB is proposed. By regulating the polarity and magnitude of FBC output voltage during the fault, the rising speed of fault current can be suppressed to reduce the breaking current of hybrid DCCB.

B. *Analysis of SP-PFC Output Voltage and Line Current*

Fig. 2 shows the interconnections among three different DC-DNs (DC1∼DC3). L_i and N_i (i = 12,3) denote the DC transmission lines and node number, respectively. The SP-PFC is adopted as the interconnections of two adjacent DC-DNs (N_1 and N_2). Since the SP-PFC plays the role of connecting two DC-DNs, its purpose is to control the constant power transfer between the two DC-DNs. Therefore, this paper adopts constant power control for SP-PFC.

The equivalent circuit between N_1 and N_2 is shown in Fig. 3(a), and the corresponding steady-state model is shown in Fig. 3(b). The line inductance is neglected in the steady-state analysis.

The parallel port of the SP-PFC is equivalent to a voltage-controlled current source, which is related to the efficiency and output voltage of the SP-PFC. A voltage source represents the series part of SP-PFC. η_p and η_n represent the efficiency of positive and negative SP-PFC, which are defined as follows:

$$\begin{cases} \eta_p = \dfrac{P_{o1}}{P_{i1}} = \dfrac{V_{kp} I_{Lp}}{V_{1p} I_{kp}} \\ \eta_n = \dfrac{P_{o2}}{P_{i2}} = \dfrac{V_{kn} I_{Ln}}{V_{1n} I_{kn}} \end{cases} \tag{1}$$

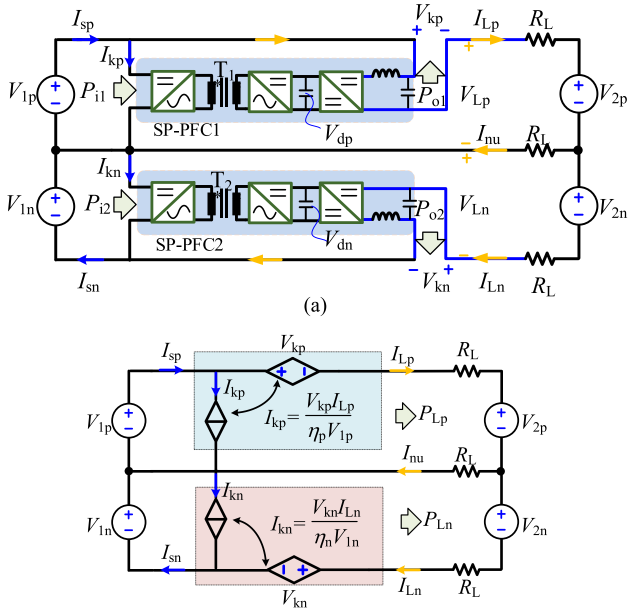

Fig. 3. Equivalent circuit of bipolar DC-DN with SP-PFC: (a) the topology of bipolar DC-DN containing SP-PFC, (b) the corresponding steady-state model.

It is assumed that the voltages of the positive and negative poles of the nodes on both sides of the SP-PFC are equal. Namely, $V_{1p} = V_{1n} = V_1$, $V_{2p} = V_{2n} = V_2$. According to Fig. 3(b), the KVL and KCL of this circuit fulfill:

$$\begin{cases} -V_1+V_{kp}+I_{Lp}R_L+V_2+I_{nu}R_L=0 \\ -V_1+V_{kn}+I_{Ln}R_L+V_2-I_{nu}R_L=0 \end{cases} \tag{2}$$

$$\begin{cases} I_{nu}=I_{Ln}-I_{Lp} \\ I_{Lp}+I_{kp}-I_{sp}=0 \\ I_{Ln}+I_{kn}-I_{sn}=0 \end{cases} \tag{3}$$

In practice, it is expected that the transmission power of the DC line is flexible and controllable between two different DC-DNs. If the constant power control is applied in SP-PFC, the power transmitted by the positive and negative poles is equal ($P_{Lp} = P_{Ln} = P$). In this situation, the current flowing through the neutral conductor is zero ($I_{nu} = 0$). Therefore, we have

$$\begin{cases} I_{Lp}V_{Lp}=I_{Lp}(V_1-V_{kp})=P \\ I_{Ln}V_{Ln}=I_{Ln}(V_1-V_{kn})=P \end{cases} \tag{4}$$

where P is the reference power of the DC transmission line. Equations (2) and (3) are rewritten as:

$$\begin{cases} -V_1+V_{kp}+I_{Lp}R_L+V_2=0 \\ -V_1+V_{kn}+I_{Ln}R_L+V_2=0 \end{cases} \tag{5}$$

$$\begin{cases} I_{Lp}+I_{kp}-I_{sp}=0 \\ I_{Ln}+I_{kn}-I_{sn}=0 \end{cases} \tag{6}$$

By substituting (4) into (5) We have $V_{kp} = V_{kn} = V_k$. Here, V_k satisfies:

$$V_k=\frac{1}{2}(V_2-\sqrt{-4PR_L+(-2V_1+V_2)^2} \tag{7}$$

It can be known from (4) that V_k presents a nonlinear relation with V_2, while V1 and V2 determine it. Since the positive and negative poles in Fig. 3(b) are entirely symmetrical, we have $I_{Lp} = I_{Ln} = I_L$, $I_{kp} = I_{kn} = I_k$, $\eta_p = \eta_n = \eta$. By substituting (6) and (7) into (5), I_L and I_k satisfy:

$$I_L=\frac{2V_1-V_2-\sqrt{-4PR_L+(-2V_1+V_2)^2}}{2R_L} \tag{8}$$

$$I_k=\frac{-2PR_L+V_1\left(2V_1-V_2-\sqrt{-4PR_L+(-2V_1+V_2)^2}\right)}{2\eta R_L V_1} \tag{9}$$

It can be seen that *V1 and V2 also determine IL*. However, I_k is related to η_p and η_n. Besides, V_k, I_L and I_k in Eqs. (8) and (9) have nonlinear relations with V_1 and V_2, which is not convenient for analyzing the relationship among different electrical quantities.

To obtain a linear relationship between different variables, Eq. (4) is transformed into:

$$\begin{cases} I_{Lp}=\frac{P}{V_{Lp}}=\frac{P}{V_1-V_{kp}} \\ I_{Ln}=\frac{P}{V_{Ln}}=\frac{P}{V_1-V_{kn}} \end{cases} \tag{10}$$

The nonlinear term $1/V_{Lp}$ in (10) is approximated using a first-order Taylor's series expansion around the operating point (V_0, I_0). Here, V_0 and I_0 are regarded as rated voltage and rated current. Such a term is selected to be linearized because V_{Lp} does not take zero values. The linearization of the term $1/V_{Lp}$ is based on the general form of the Taylor's formula for a continuous nonlinear function around (V_0, I_0) [25]. Therefore, (10) is rewritten as:

$$\begin{cases} I_{Lp}=\left[\frac{2}{V_0}-\left(\frac{1}{V_0}\right)^2 V_{Lp}\right]P \\ I_{Ln}=\left[\frac{2}{V_0}-\left(\frac{1}{V_0}\right)^2 V_{Ln}\right]P \end{cases} \tag{11}$$

Hence, (4) is linearized at the operating point ($V_0{*}I_0 = P$), which is be rewritten as:

$$\begin{cases} V_1-V_{kp}=2V_0-I_{Lp}V_0^2/P \\ V_1-V_{kn}=2V_0-I_{Ln}V_0^2/P \end{cases} \tag{12}$$

By Substituting (12) into (5), V_k, I_k, and I_L can be derived as follows:

$$\begin{cases} V_k=\frac{PR_L(-2V_0+V_1)+V_0^2(V_1-V_2)}{PR_L-V_0^2} \\ I_L=\frac{2P(-V_0+V_1-V_2)}{PR_L-V_0^2} \end{cases} \tag{13}$$

$$I_k=\frac{P\left(2V_0-2V_1+V_2\right)\left(PR_L\left(2V_0-V_1\right)+V_0^2\left(-V_1+V_2\right)\right)}{\eta(-PR_L+V_0^2)^2 V_1} \tag{14}$$

Equation (13) shows that both V_k and I_L present linear relations with V_2. Therefore, a linear relationship exists between V_k and I_L. To verify (5)–(14), the parameters in Fig. 3(b) are illustrated as follows: $R_L = 0.1\ \Omega$, $V_1 = V_0 = 350$V, $\eta = 0.85$, and $P = 10$kW. V_2 ranges from 330V to 370V. According to (5)–(14), V_k and I_k under linear and nonlinear models are shown in Fig. 4(a) and (b), respectively.

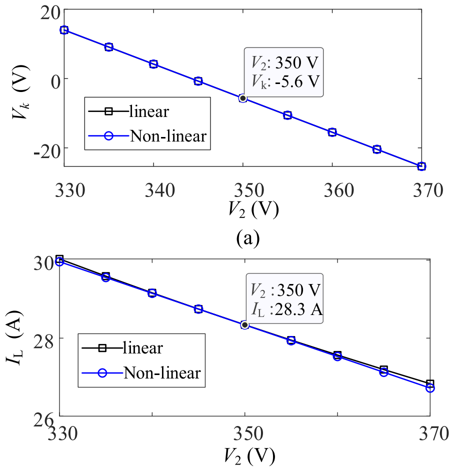

(a)

(b)

Fig. 4. Comparison of the nonlinear and linear model of SP-PFC under different V_2: (a) V_k, (b) I_L.

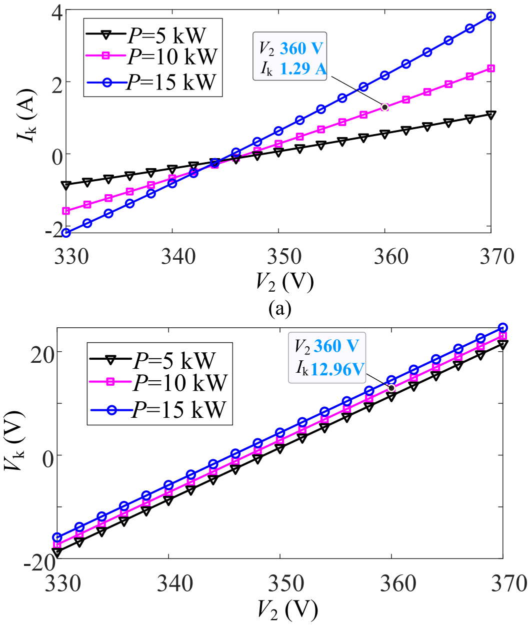

(a)

(b)

Fig. 5. The input current and output voltage of SP-PFC under different transmitted power: (a) I_k, (b) V_k.

It can be seen from Fig. 4(a) that when V_2 increases from 330V to 370V, V_k declines from +15V to -25V. The power transmitted by the line is kept as P. Furthermore, the error between the linear and nonlinear model is small. Hence, Eq. (13) can accurately reflect the variation of V_k. Fig. 4(b) presents the variations of I_L under different V_2. When V_2 is changed from 330V to 370V, I_L decreases from 30A to 27A, which means the influence percentage of V_2 variations on I_L is (27-30)/(370-330) $= -7.5\%$. This shows that when the SP-PFC connects two DC-DNs, the current variation caused by the voltage change is small. If no SP-PFC is installed, even small voltage changes can cause large current variations due to the small line resistance.

Fig. 5 illustrates the input current and output voltage of SP-PFC under different transmitted power. It can be seen that the input current of SP-PFC varies from -1.58A to 2.37A, which is less than one-tenth of the line current. In addition, the output voltage of SP-PFC is also relatively small. Therefore, the power processed by SP-PFC is far less than the rated power of the system.

C. The Influence of Unbalanced Receiving-End Voltage

In this Section, the positive and negative pole voltages of N_2 are assumed to be unbalanced. The influence of unbalanced voltage on V_kp, V_kn and I_Lp, I_Ln will be investigated. To make a comparison, the expressions of line current without SP-PFC are derived first. When there is no SP-PFC in Fig. 3(b), the KVL of this circuit is:

$$\begin{cases} -V_1 + I_{Lp}R_L + V_{2p} - (I_{Ln} - I_{Lp})R_L = 0 \\ -V_1 + I_{Ln}R_L + V_{2n} + (I_{Ln} - I_{Lp})R_L = 0 \end{cases} \tag{15}$$

By solving (15), I_Lp and I_Ln can be derived by:

$$\begin{cases} I_{Lp} = -\frac{-3V_1+2V_{2p}+V_{2n}}{3R_L} \\ I_{Ln} = -\frac{-3V_1+V_{2p}+2V_{2n}}{3RL} \end{cases} \tag{16}$$

It can be known from Eq. (16) that both I_Lp and I_Ln are related to V_2p and V_2n, and the unbalanced current ($I_\mathrm{nu} = I_\mathrm{Ln} - I_\mathrm{Lp}$) can be further derived by:

$$I_{nu} = \frac{V_{2n} - V_{2p}}{3R_L} \tag{17}$$

As shown in (17), I_nu is determined by V_2p and V_2n, and line impedance. When the difference between V_2p and V_2n is large, I_nu will be significant. This is not conducive to the safe and efficient operation of the system. When the SP-PFC is adopted as the interconnections between N_1 and N_2, I_nu can be regulated flexibly. When positive and negative pole voltages of N_2 are unbalanced, according to Fig. 3(b), (2) can be rewritten as:

$$\begin{cases} -V_1 + I_{Lp}R_L + V_{2p} + V_{kp} - (I_{Ln} - I_{Lp})R_L = 0 \\ -V_1 + I_{Ln}R_L + V_{2n} + V_{kn} + (I_{Ln} - I_{Lp})R_L = 0 \end{cases} \tag{18}$$

By solving (13), V_kp and V_kn can be derived by:

$$\begin{cases} V_{kp} = \frac{V_1\left(-3P^2R_L^2+V_1^3(V_1-V_{2p})+PR_LV_1(2V_1-2V_{2p}-V_{2n})\right)}{\left(PR_L+V_1^2\right)\left(3PR_L+V_1^2\right)} \\ V_{kn} = \frac{V_1\left(-3P^2R_L^2+V_1^3(V_1-V_{2n})+PR_LV_1(2V_1-V_{2p}-2V_{2n})\right)}{\left(PR_L+V_1^2\right)\left(3PR_L+V_1^2\right)} \end{cases} \tag{19}$$

I_Lp and I_Ln can be derived by:

$$\begin{cases} I_{Lp} = \frac{P\left(V_1^2(2V_1-V_{2p})+PR_L(6V_1-2V_{2p}-V_{2n})\right)}{\left(PR_L+V_1^2\right)\left(3PR_L+V_1^2\right)} \\ I_{Ln} = \frac{P\left(V_1^2(2V_1-V_{2n})+PR_L(6V_1-V_{2p}-2V_{2n})\right)}{\left(PR_L+V_1^2\right)\left(3PR_L+V_1^2\right)} \end{cases} \tag{20}$$

Therefore, I_nu satisfies:

$$I_{nu} = \frac{P\left(-V_{2p} + V_{2n}\right)}{3PR_L + V_1^2} \tag{21}$$

According to (16), after SP-PFC is added, I_nu is not only related to V_2p and V_2n but also influenced by P. In comparison with (17), it is equivalent to adding a resistance ($V_1{}^2/P$) to the denominator of (21). Therefore, I_nu is reduced dramatically.

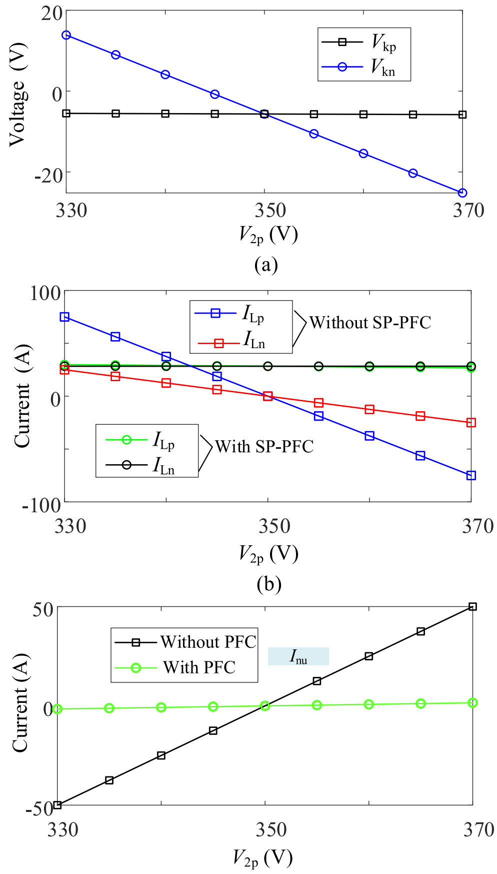

(a)

(b)

(c)

Fig. 6. Comparison of output voltage and current with or without SP-PFC: (a) output voltage, (b) line current, (c) unbalanced current.

To compare the voltage and current characteristics of SP-PFC under different cases, the parameters of Fig. 3(b) are illustrated as follows: $V_{2n} = 350$V, V_{2p} changes from 330V to 370V, and other parameters are the same as those in the above Section. V_{kp} and V_{kn} are shown in Fig. 6(a), and I_{Lp}, I_{Ln} and I_{nu} are shown in Fig. 6(b) and (c), respectively.

As shown in Fig. 6(a), when V_{2p} changes from 330 V to 370 V, V_{kp} declines from +14 V to −25 V. As V_{2n} is not changed, V_{kn} remains unchanged. According to Fig. 6(b), after the SP-PFC is kicked in, both I_{Lp} and I_{Ln} remain unchanged. However, when SP-PFC is cut-off, both I_{Lp} and I_{Ln} change with V_{2p}. It can be known from Fig. 6(c) that after SP-PFC is cut-in, I_{nu} is kept at 0; otherwise, I_{nu} will increase with V_{2p}.

D. Influence of Unbalanced Local Load on SP-PFC

When the positive and negative loads at N_1 are unbalanced, the unbalanced current will be generated in the neutral line. It can be concluded from Fig. 5(a) that the primary-side current of SP-PFC is only 1/20 of the line current. To simplify the analysis, the SP-PFC is equivalent to a series circuit of internal resistance and voltage source, and $V_{1p} = V_{1n} = V_{2p} = V_{2n} = V_s$. According to Fig. 3, the simplified equivalent circuit of bipolar DC-DN containing unbalanced local loads is shown in Fig. 7. Here, R_c denotes the internal resistance of SP-PFC, R_p and R_n represent equivalent resistances of positive and negative DC loads, respectively.

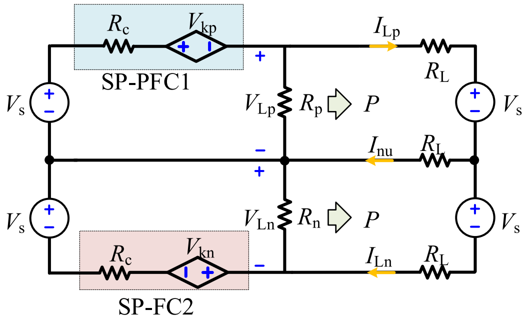

Fig. 7. The equivalent circuit of bipolar DC-DN when the local load is unbalanced.

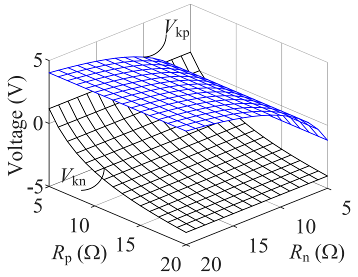

Fig. 8. The effect of unbalanced loads on the V_{kp} and V_{kn}.

According to Fig. 7, the relationships of V_{kp} and V_{kn} with R_p and R_n can be derived by:

$$\begin{cases} V_{kp} = \dfrac{P(2V_0(R_cR_L+R_p(R_c-R_L))-R_pV_s(R_c+R_L))-R_cV_0^2V_s}{R_p\left(-PR_L+V_0^2\right)} \\ V_{kn} = \dfrac{P(2V_0(R_cR_L+R_n(R_c-R_L))-R_nV_s(R_c+R_L))-R_cV_0^2V_s}{R_n\left(-PR_L+V_0^2\right)} \end{cases} \tag{22}$$

As shown in (17), V_{kp} is related to R_p, but does not relate to R_n. This means that the electrical quantities of the positive and negative poles do not affect each other. Besides, after the SP-PFC is added, I_{Lp} and I_{Ln} are equal ($I_{nu} = 0$). The expression of I_{Lp} and I_{Ln} satisfy:

$$I_{Lp} = I_{Ln} = -\frac{P\left(2V_0 - V_s\right)}{-PR_L + V_0^2} \tag{23}$$

According to (23), the unbalanced current can be suppressed effectively. Fig. 8 illustrates the variations of V_{kp} and V_{kn} under different R_p and R_n. Here, R_p and R_n vary from 5 Ω to 20 Ω, and the other parameters are the same as those in the above Section. It can be seen from Fig. 8 that when R_p increases, V_{kp} is reduced, while V_{kn} is kept unchanged. This means that the voltage on the line side can be flexibly changed according to local load changes, and the power transmitted in DC lines remains unchanged after the SP-PFC is adopted.

III. STABILITY AND DYNAMICS ANALYSIS OF BIPOLAR DC-DNS WITH SP-PFC

A. Stability Analysis of Bipolar DC-DNs With SP-PFC

A small-signal model of bipolar DC-DNs containing SP-PFC is established in this Section, which is used to analyze the

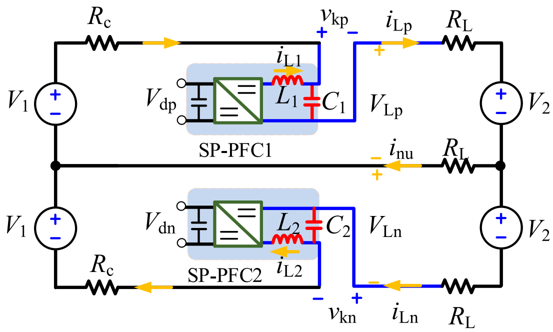

Fig. 9. A simplified model of the bipolar DC-DN containing SP-PFC.

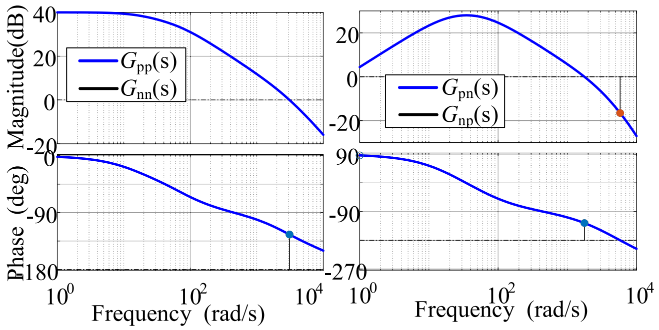

Fig. 10. The transfer functions of d_p to v_{kp} and v_{kn}: (a) $G_{pp}(s)$ and $G_{nn}(s)$, (b) $G_{pn}(s)$ and $G_{np}(s)$.

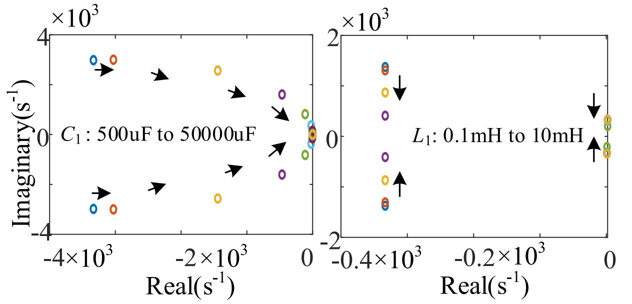

Fig. 11. The pole variations of $G_{pp}(s)$ under different C_f and L_f: (a) C_f, (b) L_f.

dynamic performance of SP-PFC and design the control parameters.

Due to the difference in control bandwidth, DAB can be equivalent to a voltage-invariant capacitive element relative to FBC in Fig. 9 [23], where C_1 and C_2, L_1 and L_2 are filter capacitances and inductance at positive and negative poles of SP-PFC, respectively; d_p and d_n denote duty cycles controlled by positive and negative poles of FBC; v_{kp} and v_{kn} are instantaneous values V_{kp} and V_{kn}, respectively. Here, we assume that $V_{dp} = V_{dn} = V_{dc}$. The inductor current (i_{L1} and i_{L2}) and capacitor voltage (v_{kp} and v_{kn}) of the FBC are selected as state variables, and the transfer function from the control variable to the state variable are derived.

As shown in Fig. 7, the relationships between I_{Lp}, I_{Ln} and V_{kp}, V_{kn} are derived by:

$$\begin{cases} I_{Lp} = b_1 V_{kp} + b_2 V_{kn} + C_0 \\ I_{Ln} = b_2 V_{kp} + b_1 V_{kn} + C_0 \end{cases} \tag{24}$$

where:

$$\begin{cases} b_1 = (R_c + 2R_L)/Z_0 \\ b_2 = R_L/Z_0 \\ C_0 = (R_c + 3R_L)(V_1 - V_2)/Z_0 \\ Z_0 = R_c^2 + 4R_cR_L + 3R_L^2 \end{cases} \tag{25}$$

Equation (24) illustrates the relations between the output voltage of SP-PFC and the line current. On this basis, the relationship between the inductance current and the output voltage of SP-PFC (V_{kp} and V_{kn}) can be obtained. The state equation in Fig. 3(b) can be derived by taking SP-PFC output voltage and inductance current as the state variables, which fulfills:

$$\begin{cases} C_1 \frac{dv_{kp}}{dt} = i_{L1} - i_{p2} = i_{L1} - b_1 V_{kp} - b_2 V_{kp} - C_0 \\ C_2 \frac{dv_{kn}}{dt} = i_{L2} - i_{n2} = i_{L2} - b_2 V_{kp} - b_1 V_{kn} - C_0 \\ L_1 \frac{di_{L1}}{dt} = 2d_p V_{dc} - V_{kp} \\ L_2 \frac{di_{L2}}{dt} = 2d_n V_{dc} - V_{kn} \end{cases} \tag{26}$$

According to (26), the system state equation can be expressed as below:

$$\dot{x} = Ax + Bu \tag{27}$$

where

$$\begin{cases} \mathrm{A} = \begin{bmatrix} -b_1/C_1 & -b_2/C_1 & 1/C_1 & 0 \\ -b_2/C_2 & -b_1/C_2 & 0 & 1/C_2 \\ -1/L_1 & 0 & 0 & 0 \\ 0 & -1/L_2 & 0 & 0 \end{bmatrix} \\ \mathrm{B} = \begin{bmatrix} 0 & 0 & 2V_{dc}/L_1 & 0 \\ 0 & 0 & 0 & 2V_{dc}/L_2 \end{bmatrix}^{\mathbf{T}} \\ \mathrm{x} = \begin{bmatrix} v_{kp} & v_{kn} & i_{L1} & i_{L2} \end{bmatrix}^{\mathbf{T}} \\ \mathrm{u} = \begin{bmatrix} d_p & d_n \end{bmatrix}^{\mathbf{T}} \end{cases} \tag{28}$$

The input-to-output transfer function can be derived according to (27) and (28). It can be found that this system is a double-input and double-output system. The transfer functions of d_p to v_{kp} and v_{kn} satisfy:

$$\begin{cases} G_{pp}(s) = \frac{\hat{v}_{kp}}{\hat{d}_p}\big|_{\hat{d}_n(s)=0} = \frac{N_{pp}(s)}{D(s)} \\ N_{pp}(s) = 2V_{dc}\left(1 + b_1 Ls + CLs^2\right) \\ D(s) = 1 + 2b_1 Ls + \left(2CL + L^2(b_1^2 - b_2^2)\right) s^2 \\ +2b_1 CL^2 s^3 + C^2 L^2 s^4 \end{cases} \tag{29}$$

$$\begin{cases} G_{pn}(s) = \frac{\hat{v}_{kp}}{\hat{d}_n}\big|_{\hat{d}_p(s)=0} = \frac{N_{pn}(s)}{D(s)} \\ N_{pn}(s) = 2V_{dc} b_2 Ls \end{cases} \tag{30}$$

The transfer functions of d_n to v_{kp} and v_{kn} are represented by $G_{np}(s)$ and $G_{nn}(s)$, respectively. When the bipolar DC-DN is in balanced state, we have $G_{pp}(s) = G_{nn}(s)$ and $G_{pn}(s) = G_{np}(s)$.

B. Dynamic Analysis of Bipolar DC-DNs Containing SP-PFC

According to Eqs. (27) and (28), the Bode graphs of G_{pp}(s), $G_{nn}(s)$, G_{pn}(s) and $G_{np}(s)$ are shown in Fig. 10. Here, $R_c = 0.01$ Ω, $R_L = 0.1$ Ω, $V_1 = 350$ V, $V_2 = 345$ V, $C_1 = C_2 = C_f = 5$ mF, $V_{dc} = 50$ V and $L_1 = L_2 = L_f = 1$ mH. As shown in Fig. 10, the phase margin of G_{pp}(s) and $G_{nn}(s)$ is 54.6°. Therefore, the closed-loop stability of $G_{pp(}$s) and G_{nn}(s) can be guaranteed. It

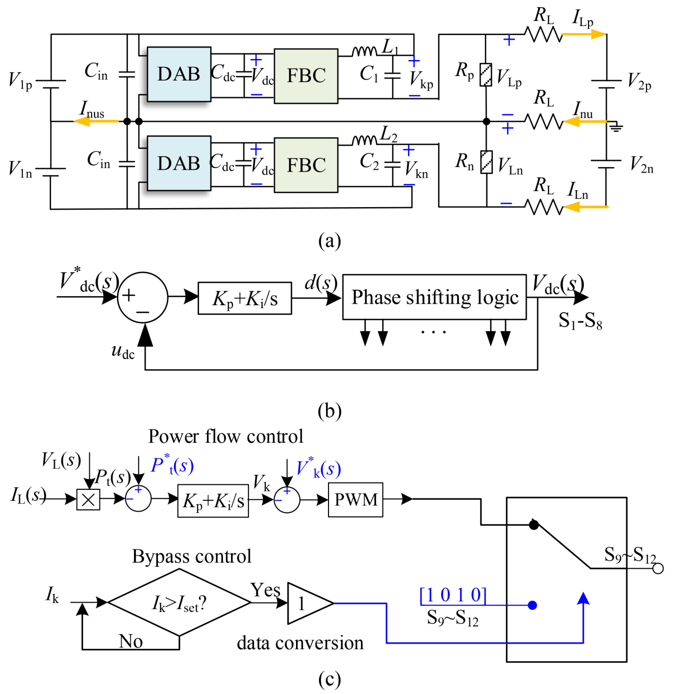

Fig. 12. The simulation setup: (a) the schematic of simulation, (b) control of DAB, (c) control of FBC.

can be seen from Fig. 10(b) that the positive and negative poles are coupled, which is consistent with the previous analysis.

To further analyze the influence of circuit parameters on the system stability, the impacts of C_f and L_f on system poles are analyzed, where C_f changes from 0.5 mF to 50 mF, and L_f from 0.1 mH to 10 mH [26]. The other parameters are consistent with part B of Section II. The pole variations of $G_{pp}(s)$ are shown in Fig. 11. It can be seen that all of the poles are on the left plane. Therefore, the change of C_f and L_f will not influence the stability of the bipolar DC-DN containing SP-PFC.

According to the transfer functions of $G_{pp}(s)$ and $G_{nn}(s)$, the proportional and integral control parameters of FBC can be quantitatively calculated. The specific parameter design method can refer to [19], [23].

IV. SIMULATION AND RESULTS

In order to verify the effectiveness of the proposed method, a simulation model of bipolar DC-DN shown in Fig. 12(a) is established in MATLAB/Simulink. Under the initial state, $V_{2p} = V_{2n} = 350$ V, $R_c = 0.01\ \Omega$, $R_L = 0.1\ \Omega$, the power (P) transmitted by the line is 10 kW. Other parameters are seen in Table I.

In this study, the control method of DAB is shown in Fig. 12(b). Here, V^*_{dc} represents the reference value of V_{dc}. K_p and K_i are proportionality and integral coefficients; d is the duty ratio of DAB. The constant voltage control is applied in DAB, which makes the V_{dc} a constant value. The control method of FBC is shown in Fig. 12(c). Here, V_L, I_L, and P_t are voltage, current, and transmitted power of the DC transmission line, respectively. P^*_t and V^*_k are reference values of P_t and V_k, respectively. V_{set} is the upper limit of V_k.

TABLE I
PARAMETERS OF BIPOLAR DC DISTRIBUTION NETWORKS WITH SP-PFC

Parameter	Symbol	Value
DC bus voltage	$V_{1p}=V_{1n}=V_s$	350 V
DC bus voltage	$V_{2p}=V_{2n}=V_s$	350 V
Local DC load	R_p, R_n	40 Ω
Filter capacitor	C_1, C_2	5 mF
Filter inductance	L_1, L_2	1 mH
Controller parameters	K_p, K_i	0.3, 50

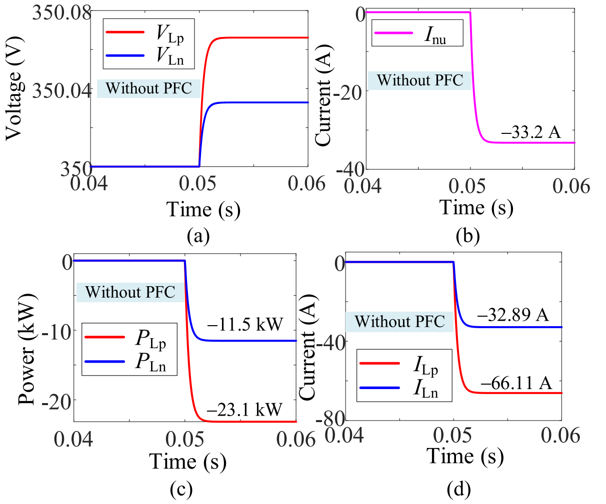

Fig. 13. The simulation results under unbalanced receiving-end voltage without SP-PFC: (a) V_{Lp} and V_{Ln}, (b) I_{nu}, (c) P_{Lp} and P_{Ln}, (d) I_{Lp} and I_{Ln}.

During normal operation, the constant power control strategy is adopted for FBC, aiming to make the power transmitted by the DC transmission line constant. When no intervention of the PFC is required, the FBC enters the bypass mode. When the bypass control is input, S_9 and S_{11} in Fig. 1 is switched on, and S_{10} and S_{12} are blocked. In this paper, when $I_k > I_{set}$, the bypass control of SP-PFC will be triggered. In this paper, I_{set} is twice the rated current.

A. *Simulation Results Under Unbalanced Receiving-End Voltage*

1) Simulation Results Under Unbalanced Receiving-End Voltage: Fig. 13 shows the simulation results without SP-PFC when V_{2p} changes from 350 V to 360 V at 0.05 s. According to Fig. 13(a), the positive and negative voltages are almost equal, which means the line voltage is not regulated. Fig. 13(b) presents that the natural line current is very large at −33.2 A after 0.05 s. Fig. 13(c) illustrates that the positive and negative transmission powers are not correlated when V_{2p} changes at 0.05 s. Fig. 13(d) shows that the positive and negative line currents are significantly changed.

V_{2p} changes from 350 V to 360 V at 0.05 s and the corresponding simulation result with SP-PFC is shown in Fig. 14. It can be known from Fig. 14(a) that both P_{Lp} and P_{Ln} are kept at 10 kW, and both of them are not influenced by V_{2p}. Fig. 14(b) shows that V_{Lp} changes from 353.2 V to 362.66 V, and its variation is

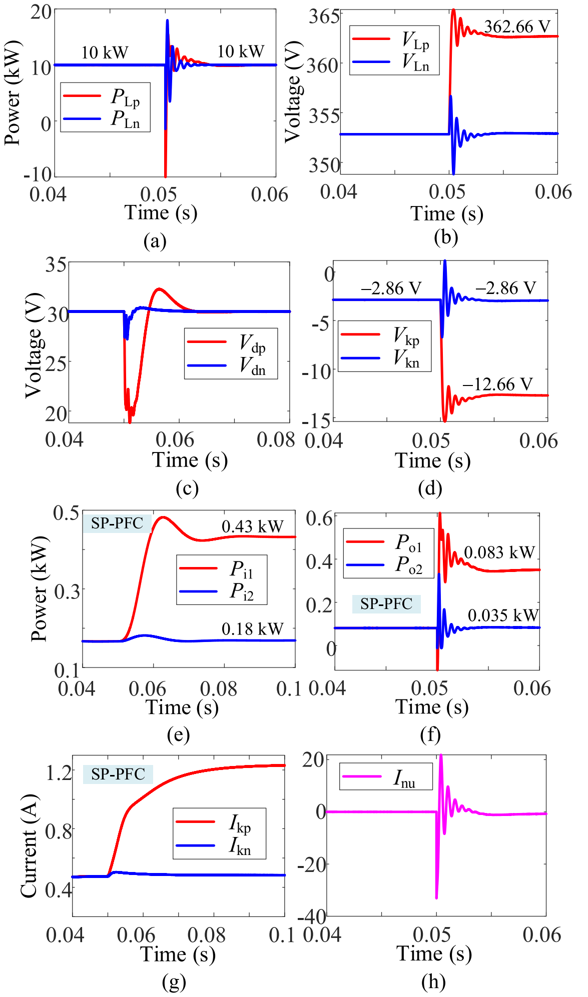

Fig. 14. The simulation results under unbalanced receiving-end voltage with SP-PFC: (a) P_{Lp} and P_{Ln}, (b) V_{Lp} and V_{Ln}, (c) V_{dp} and V_{dn}, (d) V_{kp} and V_{kn}, (e) P_{i1} and P_{i2}, (f) P_{o1} and P_{o2}, (g) I_{kp} and I_{kn}, (h) I_{nu}.

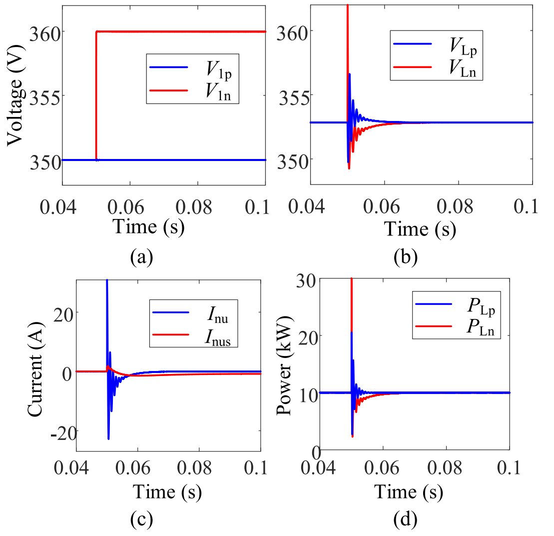

Fig. 15. The transmission characteristics of unbalanced voltage in the bipolar DC-DNs with SP-PFC: (a) V_{1p} and V_{1n}, (b) V_{Lp} and V_{Ln}, (c) I_{nu} and I_{nus}, (d) P_{Lp} and P_{Ln}.

consistent with V_{2p}. Therefore, SP-PFC can flexibly adjust the output voltage to keep the transmission power of the DC line constant. At the same time, the control degree of freedom of the toroidal bipolar DC system has also increased. In Fig. 14(c), V_{dp} and V_{dn} represent the positive and negative output voltage of DAB, respectively. It can be seen that V_{dp} and V_{dn} are kept at 30 V. Therefore, this proves that the primary side of SP-PFC has the characteristics of rated voltage and partial current, and the secondary side has the characteristics of partial voltage and rated current. Fig. 14(d) illustrates that the amplitudes of the positive and negative output voltage of SP-PFC are always small than the secondary-side voltage of DAB.

Fig. 14(e) illustrates the input power of SP-PFC. P_{i1} and P_{i2} also smaller than 0.5 kW. This proves that SP-PFC only needs to deal with the partially rated power of the system. Fig. 14(f) shows the output power of SP-PFC. It can be seen that P_{o1} and P_{o2} are smaller than 0.5 kW under the unbalanced receiving-end voltage. This power is only one-twentieth of the rated power of the system. Fig. 14(g) shows the current of SP-PFC. When V_{2p} changes, I_{kp} changes with it to keep the power of the DC line constant. Fig. 14(h) shows the unbalanced current of the bipolar DC network (I_{nu}). I_{nu} is kept at 0A, which is consistent with the previous analysis. This means that SP-PFC can effectively suppress the unbalanced power of the system.

To investigate the transmission characteristics of unbalanced voltage, V_{1p} increases from 350 V to 360 V at 0.05 s. Fig. 15(a) presents that only the voltage of V_{1p} changes from 350 V to 360 V while V_{1n} remains the same. Fig. 15(b) illustrates that the positive and negative line voltage will not be influenced by the change of V_{1p}, which means the unbalanced voltage will not be transmitted. Fig. 15(c) shows that the neutral line current I_{nus} changes slightly due to the change of V_{1p}. It can be seen from the topology in Fig. 12(a) that there is no neutral line resistance in the left side of SP-PFC, which means the change of I_{nus} will not influence the power losses of the bipolar DC-DN. According to Fig. 15(d), the positive and negative transmission power is stable at 10 kW under the unbalanced voltage of V_{1p}.

2) Simulation Results Under Unbalanced Local Load: At 0.05s, a DC load with 20 Ω is input to node N_1, and the simulation results are shown in Fig. 16. It can be known from Fig. 16(a) that P_{Lp} and P_{Ln} are kept at 10 kW. Besides, the line voltages V_{P} and V_{N} are kept at 353V, and the change of DC loads influences neither of them. Since P_{Lp} and P_{Ln} are always equal, $I_{\text{nu}} = 0$. Therefore, the SP-PFC can inhibit the unbalanced current generated by unbalanced DC loads. Fig. 16 also presents the output voltage and processed power of the SP-PFC. It can be seen that the output voltage of the SP-PFC is small, and the processed power is only 5% of the rated power. Therefore, the SP-PFC is cost-effective.

3) Simulation Results When the Power Flow Is Reversed: When there is SP-PFC in the network, the power flow direction can be flexibly controlled. Fig. 17 shows the transient response of SP-PFC when the power flow is reversed. At 0.05 s, the reference value of the line power is changed from 10 kW to −10 kW, as

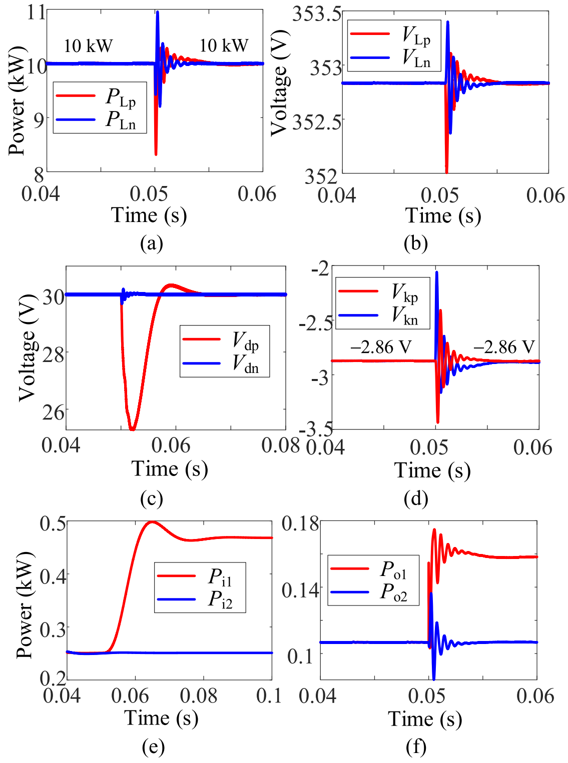

Fig. 16. The simulation results under unbalanced local load: (a) P_{Lp} and P_{Ln}, (b) V_{Lp} and V_{Ln}, (c) V_{dp} and V_{dn}, (d) V_{kp} and V_{kn}, (e) P_{i1} and P_{i2}, (f) P_{o1} and P_{o2}.

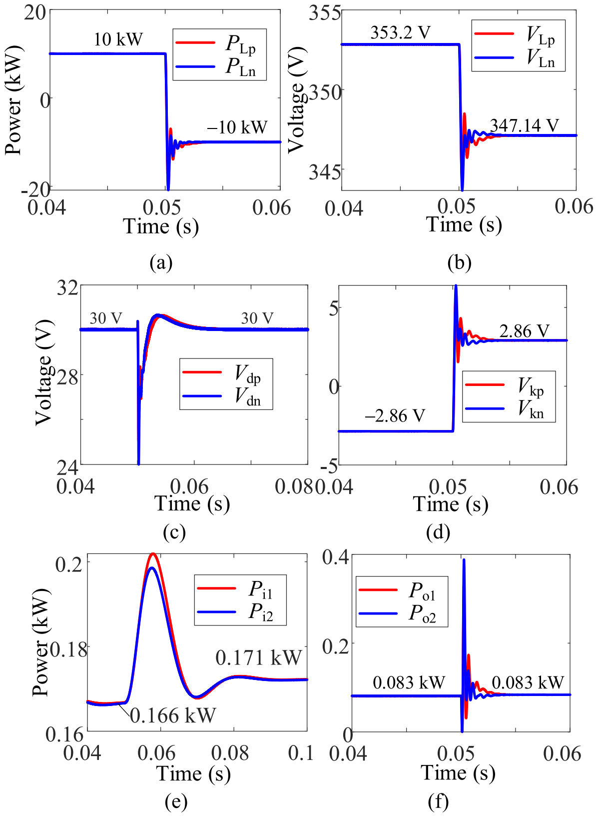

Fig. 17. The simulation results when the power flow is reversed: (a) P_{Lp} and P_{Ln}, (b) V_{Lp} and V_{Ln}, (c) V_{dp} and V_{dn}, (d) V_{kp} and V_{kn}, (e) P_{i1} and P_{i2}, (f) P_{o1} and P_{o2}.

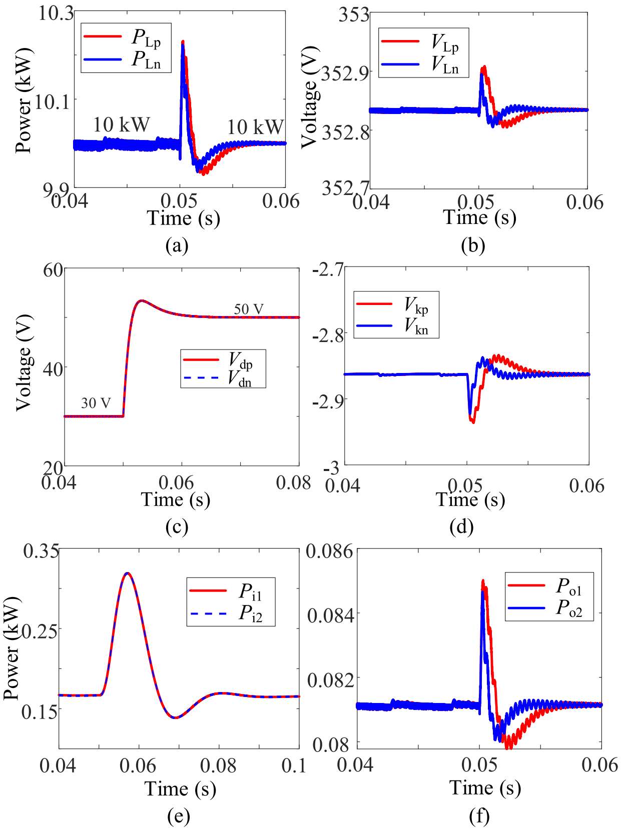

Fig. 18. The simulation results when the reference voltage of DAB changes: (a) P_{Lp} and P_{Ln}, (b) V_{Lp} and V_{Ln}, (c) V_{dp} and V_{dn}, (d) V_{kp} and V_{kn}, (e) P_{i1} and P_{i2}, (f) P_{o1} and P_{o2}.

shown in Fig. 17(a). It can be seen that the line voltage (V_{Lp} and V_{Ln}) and the output voltage of SP-PFC (V_{kp} and V_{kn}) are reversed, which makes the power flow bidirectional. However, the output voltage and input power of DAB are kept unchanged, which means the power processed by SP-PFC is still low.

4) Simulation Results When the Reference Voltage of DAB Changes: Fig. 18 illustrates the transient response of SP-PFC when the reference voltage of DAB changes. It can be seen that except for the change in the reference voltage of DAB, the power transmitted by the line and the output voltage of the power flow controller have not changed.

B. Comparison With Other Power Flow Controller

The topology of parallel PFC (P-PFC) is shown in Fig. 19. For P-PFC, the voltage on the secondary side is the same as that on the line side. Therefore, the P-PFC can flexibly adjust the voltage on the line side, and the power transmitted by the line and the simulation results are shown in Fig. 20, where (a) and (b) show that the input and output power of P-PFC is rated at 10 kW under the unbalanced voltage of $V_{2\mathrm{p}}$ at 0.15 s. Fig. 20(c) and (d) present the ability of the P-PFC to adjust the unbalanced voltage and current. The positive and negative voltages of P-PFC are both 353 V, and the positive and negative current is 28.3 A when the change of $V_{2\mathrm{p}}$ at 0.15 s.

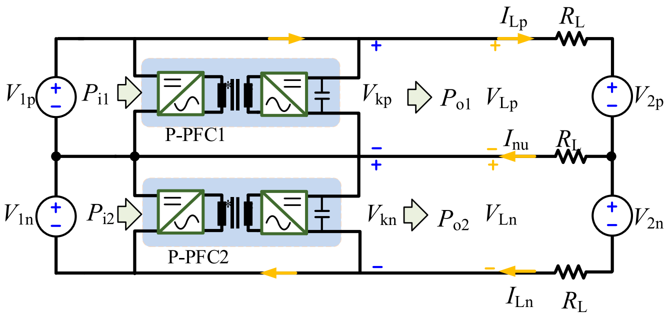

Fig. 19. The topology of bipolar DC-DN containing P-PFC.

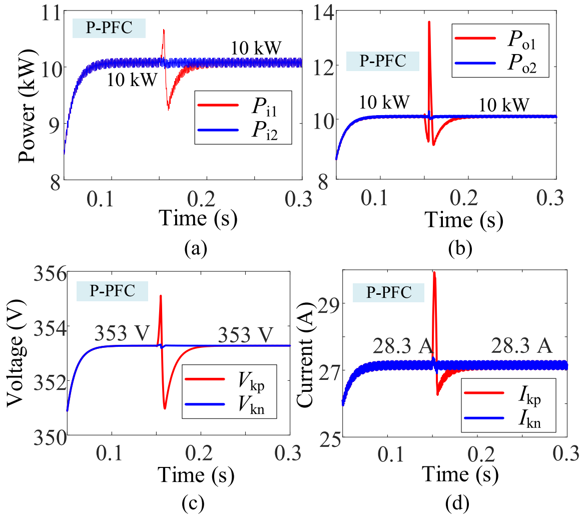

Fig. 20. The simulation results under unbalanced receiving-end voltage with P-PFC: (a) P_{i1} and P_{i2}, (b) P_{o1} and P_{o2}, (c) V_{kp} and V_{kn}, (d) I_{Lp} and I_{Ln}.

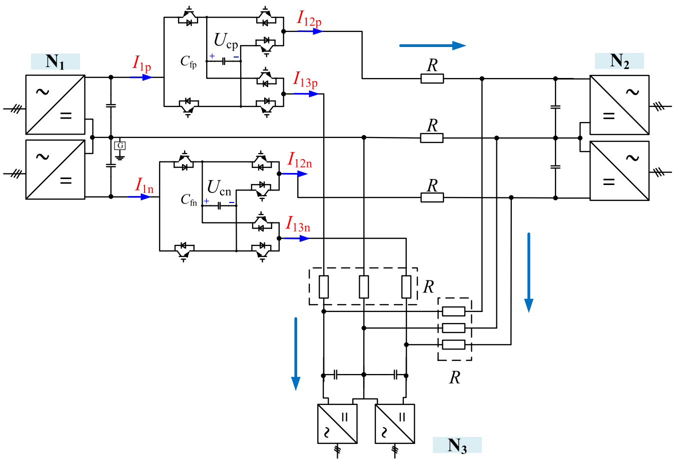

Fig. 21. The topology of the three-terminal ring bipolar DC grid with S-PFC.

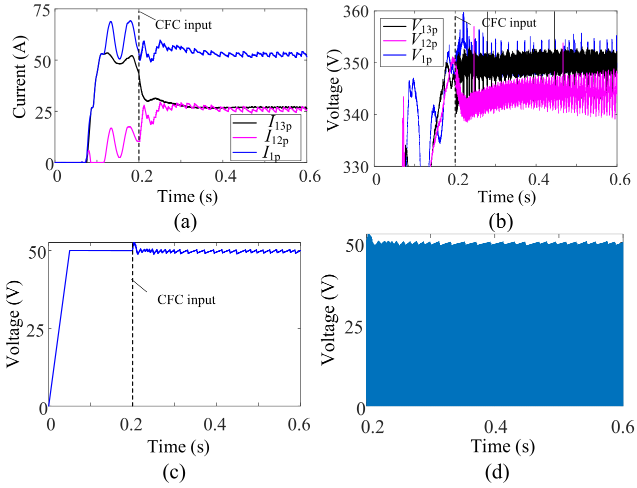

Fig. 22. The simulation results of bipolar DC-DN with S-PFC when CFC is involved: (a) $I_{13\mathrm{p}}$, $I_{12\mathrm{p}}$, and $I_{1\mathrm{p}}$, (b) $V_{13\mathrm{p}}$, $V_{12\mathrm{p}}$, and $V_{1\mathrm{p}}$ (c) voltage of C_{fp} (d) voltage of S-PFC.

According to the simulation results in Fig. 20, the P-PFC can flexibly control the voltage. However, the output voltage of the P-PFC is almost equal to the line voltage 350V, and the input current is more than 50 times that of the SP-PFC. Therefore, the P-PFC needs to deal with the rated voltage and rated power, greatly improving the requirements for the withstand voltage level and overcurrent level of the equipment and increasing the cost consumption.

The topology of the three-terminal ring bipolar DC grid with series PFC (S-PFC) is shown in Fig. 21. To verify the performance of S-PFC, the simulation results are shown in Fig. 22 when the current flow controller (CFC) is input at node N_1 at 0.2s. The transmission line resistances are both R and other related parameters are the same as those in part A. Fig. 22(a) illustrates the positive input and output current of S-PFC. The input current is 50A, equal to the output current from N1 to N2 and N3. Fig. 22(b) presents the bus voltage of the three-terminal ring bipolar DC grid, which is around 350V at the rated voltage. Fig. 22(c) and (d) respectively show the voltage of C_{fp} and S-PFC, both 50V.

In the topology of S-PFC, only the safety level of high current needs to be considered. Compared with P-PFC, the power of S-PFC is nearly 1.2kW, which is one-eighth of that of P-PFC. The protection level requirements of S-PFC are significantly reduced, and the cost is also reduced. However, under the structure of S-PFC, many ripples will be introduced, which can be seen in Fig. 22.

C. Analysis of Power Losses With and Without SP-PFC

To analyze the power losses of the network, a three-terminal ring bipolar DC grid is selected as the research object, as shown in Fig. 23(a). The length of DC transmission line is assumed to be the same, and the equivalent resistances are all R. The power losses of the network can be obtained by calculating the current flowing through the lines. When $V_{1\mathrm{p}}$ and $V_{1\mathrm{n}}$ vary between 330 V and 370 V, the power losses of the three-terminal ring bipolar DC grid are shown in Fig. 23(b). It is indicated that the addition of SP-PFC can significantly reduce the transmission line losses when there is an unbalance in the bipolar DC grid.

Fig. 24 shows the change of neutral current of three nodes with and without SP-PFC in the three-terminal ring bipolar DC

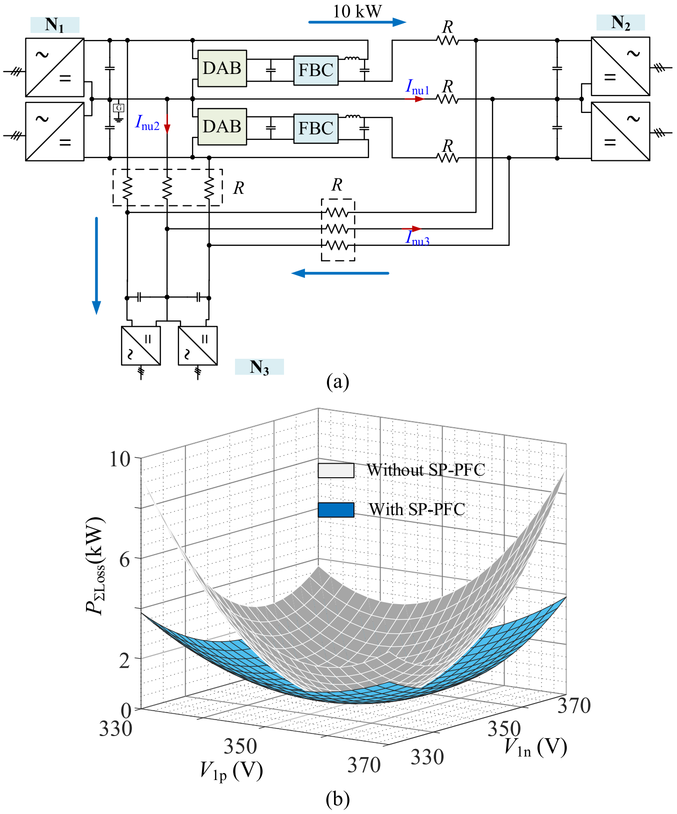

(a)

(b)

Fig. 23. Power losses analysis of three-terminal ring bipolar DC grid: (a) the topology, (b) the power losses.

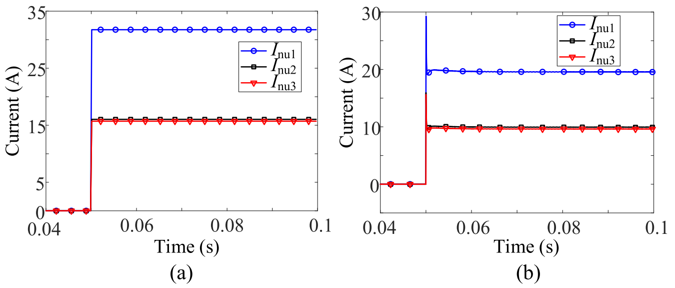

(a)

(b)

Fig. 24. The change of neutral current of three nodes (a) without and (b) with SP-PFC in the three-terminal ring bipolar DC grid.

grid. At 0.05s, the positive pole voltage of N_2 is changed from 400 V to 410 V. The directions of different neutral line currents are shown in Fig. 23(a). By comparing Fig. 24(a) and (b), it can be concluded that SP-PFC can reduce the neutral current, which is consistent with the analysis of power losses.

D. Influence of Grounding Topologies and Locations

1) Impact of Different System Configurations: The three different system configurations are presented in Fig. 25. The influence of different system configurations on the three-terminal ring bipolar DC grid with SP-PFC is investigated in this case, shown in Fig. 26. At 0.05s, the positive pole voltage of N_2 is changed from 400 V to 410 V. As seen, the symmetric monopolar without a neutral line has the maximum variation of positive and negative voltage, which is 363V and 358V, respectively. The bipolar configuration with a neutral line has the minimum positive and negative voltage variation, which is 357.8V and 352.6V, respectively. The positive and negative transmission power is, however, not affected, which is the 10 kW at the rated load.

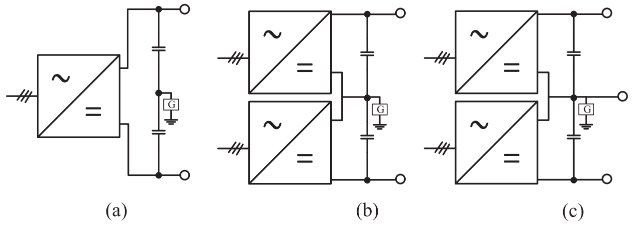

(a) (b) (c)

Fig. 25. Different system configurations: (a) symmetric monopolar without neutral line, (b) bipolar configuration without neutral line, and (c) bipolar configuration with neutral line.

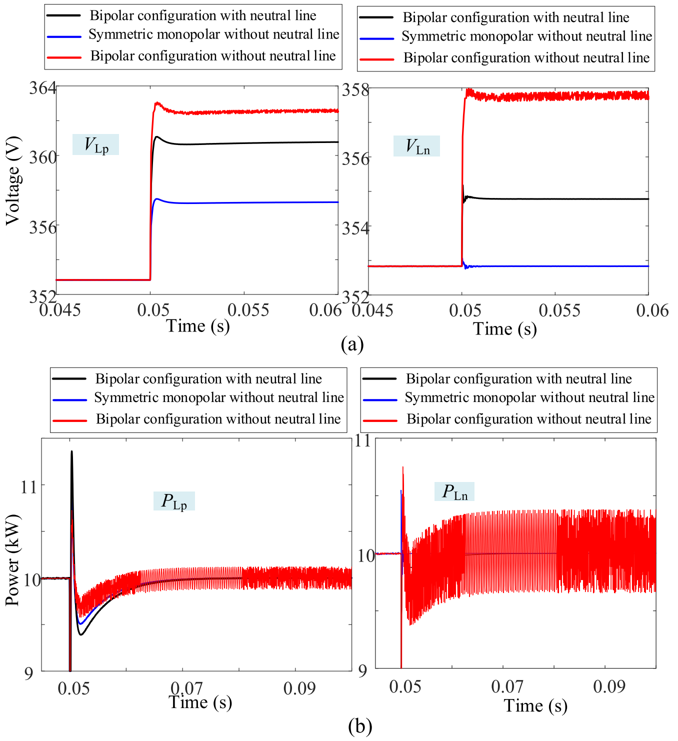

(a)

(b)

Fig. 26. The influence of three different system configurations on (a)V_{Lp} and V_{Ln} and P_{Lp} and P_{Ln}.

2) Impact of Number and Location of Grounding Points: Fig. 27 shows the effects of the number of grounding points on the positive and negative bus voltage and power. As shown in Fig. 27(a), if N_1 is solid grounded, the change of V_{Lp} and V_{Ln} is the same. If N_1 is not grounded, the change of V_{Lp} is the largest, and the change of V_{Ln} is almost unchanged. According to Fig. 27(b), if N_1 is solid grounded, the change of P_{Lp} and P_{Ln} is the same. However, the transmission power of the line will reach 10kW in all three cases. If N1 is not grounded, the

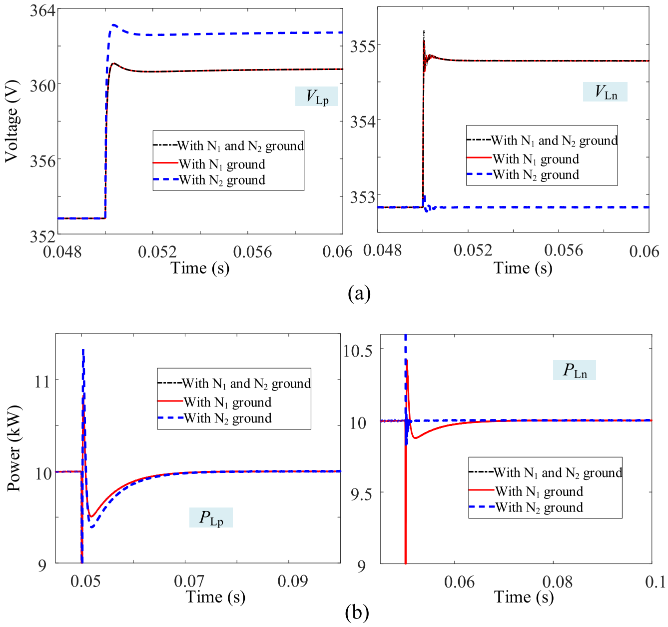

(a)

(b)

Fig. 27. The effects of the number and locations of grounding points on (a) V_{Lp} and V_{Ln} and (b) P_{Lp} and P_{Ln}.

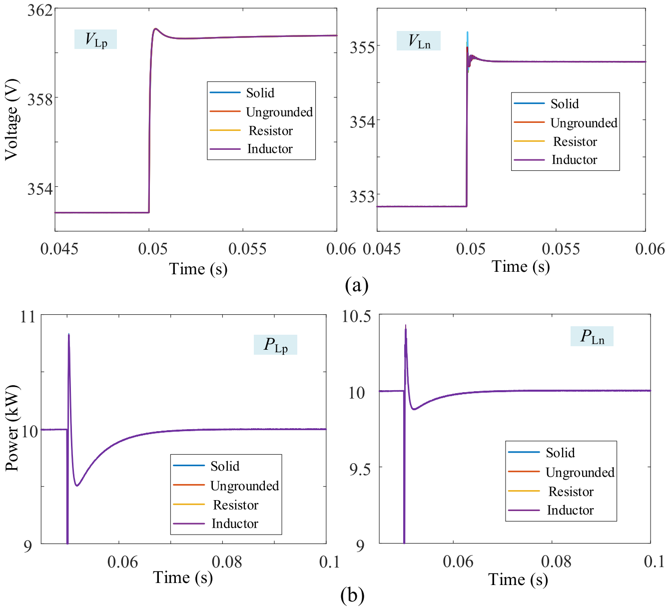

(a)

(b)

Fig. 28. The effects of the grounding practices on (a) V_{Lp} and V_{Ln} and (b) P_{Lp} and P_{Ln}.

dynamic response characteristics of P_{Lp} will be slower and the dynamic characteristics of P_{Ln} will be faster.

3) Impact of Different Grounding Practices: When the system is grounded at only one point, the characteristics of voltage and transmission power are investigated. At 0.05s, the positive pole voltage of N_2 is changed from 400 V to 410 V. Four different grounding practices are selected, and the corresponding simulation results are shown in Fig. 28. Here, the grounding resistor is 1 Ω, and the grounding inductor is 1 mH. The system is grounded at the neutral point of N_1. It can be seen from Fig. 28 that when the system has only one grounding point, no matter which grounding method is used, the result of its dynamic response is the same. Even if the ground point is changed to N_2 or N_3, the same conclusion will be drawn.

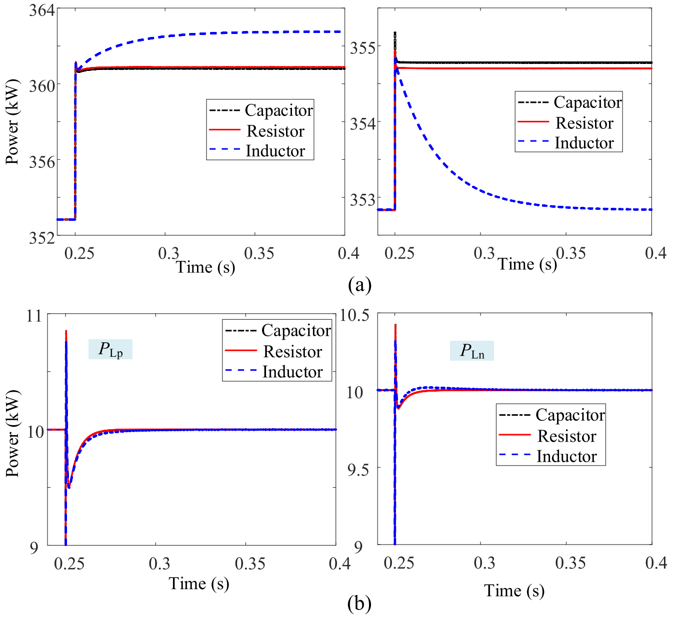

(a)

(b)

Fig. 29. The effects of grounding practices on (a) V_{Lp} and V_{Ln} and (b) P_{Lp} and P_{Ln}.

TABLE II
PARAMETERS OF EXPERIMENT PLATFORM

Parameters	value	Parameters	value
DC bus voltage	12V	Receiving end voltage	11.6V
Line resistance	2Ω	Filter inductance L_{f1},L_{f2}	1mH
Lin inductance	360μH	Filter capacitor C_{f1},C_{f2}	10μF
Local load	20Ω	Local input load R_{o}	10Ω

However, the conclusion in Fig. 29 no longer holds when the system has multiple grounding points. The system is grounded at N_1 and N_2, and N_1 is solid ground. When N_2 is grounded though different elements, the corresponding results are shown in Fig. 29. Here, the capacitor is 50 μF, and the resistor and inductor have the same value with previous analysis. It can be found that the results of capacitive grounding and resistive grounding are the same, while the inductive grounding method will significantly reduce the dynamic response speed of the system. Besides, all three practices will bring the system into steady state.

E. Experiment Verification

To verify the effectiveness of the unbalanced power flow suppression strategy proposed in this paper, an experimental platform for the bipolar DC distribution network with SP-PFC is built, as shown in Fig. 30. The experimental platform parameters are shown in Table II. SP-PFC adopts STM32H750 control. Local loads are mainly constant impedance loads in the ring-shaped bipolar DC distribution network. The reference

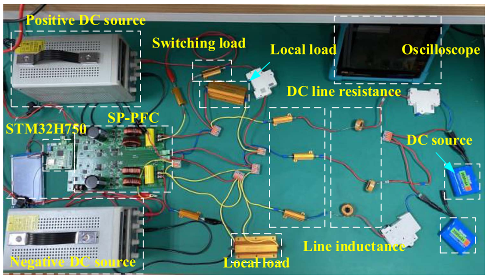

Fig. 30. The experimental platform for the bipolar DC distribution network with SP-PFC.

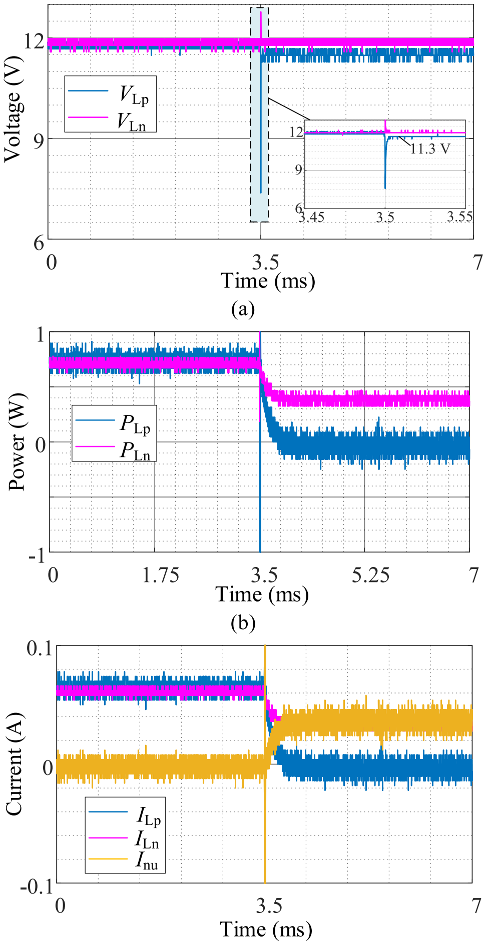

(a)

(b)

(c)

Fig. 31. The experimental results of the bipolar DC distribution network without SP-PFC under the unbalanced DC loads: (a) V_{Lp} and V_{Ln}, (b) P_{Lp} and P_{Ln}, (c) I_{Lp}, I_{Ln}, and I_{Ln}.

rated power of the transmission line is 15W. The local load is a constant resistive load, and the initial positive and negative load equivalent resistance is 20Ω. The equivalent resistance of the switching load is 10Ω.

Fig. 31 presents the experimental results of the bipolar DC distribution network without SP-PFC under the unbalanced DC loads. It can be seen from Fig. 31(a) that the positive and negative bus voltage will not return to the rated voltage after the change of receiving-end voltage. The positive bus voltage is more influenced and drops to 11.3V. Fig. 31(b) illustrates that the positive and negative transmission power will decrease due to the unbalanced receiving-end voltage. Moreover, the transmission power will not return to the rated power at 15W. Fig. 31(c) presents the positive, negative, and neutral line current. The neutral line current will not be zero, which means the unbalanced power flow is not regulated in the bipolar DC distribution network without SP-PFC.

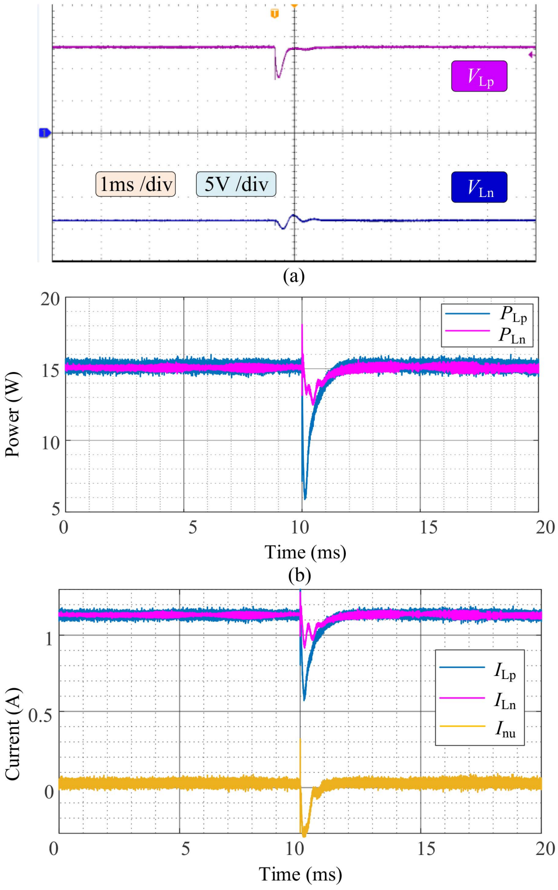

(a)

(b)

(c)

Fig. 32. Experimental result when there is local load switching: (a) V_{Lp} and V_{Ln}, (b) P_{Lp} and P_{Ln}, (c) I_{Lp}, I_{Ln} and I_{nu}.

Fig. 32 shows the steady-state experiment results (first 10ms). The magnitude of the positive and negative voltages is equal, and the voltage amplitude is close to 13V. The power transmitted by the DC line is 15W, equal to the reference rated power. Therefore, the SP-PFC allows the transmission power of the line to be flexibly controlled. The neutral line current is zero, consistent with the previous analysis. Therefore, SP-PFC can effectively suppress the unbalanced current of the bipolar DC distribution system.

The experimental result with local load switching is shown in Fig. 32. It can be seen that the positive and negative line voltages are quickly adjusted to the rated voltage after being disturbed. The transmission power of the line is still maintained at 15W, which means that SP-PFC can suppress the disturbance of local load switching.

V. CONCLUSION

An unbalanced power control strategy based on SP-PFC is proposed for the bipolar DC-DN. The SP-PFC is adopted as the interconnection between two different DC-DNs. When the SP-PFC is controlled with constant power, the unbalanced current in the neutral line can be suppressed significantly. The SP-PFC can be equivalent to a voltage source inserted into the line, and the PF can be regulated flexibly. The expressions of SP-PFC output voltage and line current are derived in this paper. Moreover, the characteristics of SP-PFC in the suppression of unbalanced receiving-end voltage unbalance and DC loads are analyzed. These analyses are helpful to understand the application of SP-PFC in suppressing the unbalanced power of bipolar DC-DN. The simulation results indicate that after the SP-PFC is added to the DC line, the power transmitted by the DC line is always unchanged. Furthermore, the output voltage of SP-PFC is small, and the processed power is only about 5% of the rated power. Therefore, the initial investment of SP-PFC has advantages over other PFCs.

REFERENCES

[1] P. Chen and X. Chen, "Error estimation method of Reduced-order Small-signal model for Multi-terminal DC distribution network," *IEEE J. Emerg. Sel. Topics Power Electron.*, vol. 9, no. 6, pp. 7212–7222, Dec. 2021, doi: 10.1109/JESTPE.2020.2998528.

[2] D. Wang, V. Psaras, A. A. S. Emhemed, and G. M. Burt, "A novel fault Let-through energy based fault location for LVDC distribution networks," *IEEE Trans. Power Del.*, vol. 36, no. 2, pp. 966–974, Apr. 2021, doi: 10.1109/TPWRD.2020.2998409.

[3] Y. Wang *et al.*, "A practical DC fault ride-through method for MMC based MVDC distribution systems," *IEEE Trans. Power Del.*, vol. 36, no. 4, pp. 2510–2519, Aug. 2021, doi: 10.1109/TPWRD.2020.2999466.

[4] F. Qiao and J. Ma, "Coordinated voltage/var control in a hybrid AC/DC distribution network," *IET Gener., Transmiss. Distrib.*, vol. 14, no. 11, pp. 2129–2137, 2020, doi: 10.1049/iet-gtd.2019.0390.

[5] Y. Tian, D. Zhao, T. Hong, and B. Cui, "Cost and efficiency analysis for hybrid AC/DC distribution system planning with PV and battery," in *Proc. IEEE Power Energy Soc. Innov. Smart Grid Technol. Conf.*, 2020, pp. 1–5, doi: 10.1109/ISGT45199.2020.9087780.

[6] X. Zhong, M. Zhu, Y. Chi, S. Liu, and X. Cai, "Composite DC power flow controller," *IEEE Trans. Power Electron.*, vol. 35, no. 4, pp. 3530–3542, Apr. 2020, doi: 10.1109/TPEL.2019.2936773.

[7] O. Gomis-Bellmunt, J. Sau-Bassols, E. Prieto-Araujo, and M. Cheah-Mane, "Flexible converters for meshed HVDC grids: From flexible AC transmission systems (FACTS) to flexible DC grids," *IEEE Trans. Power Del.*, vol. 35, no. 1, pp. 2–15, Feb. 2020, doi: 10.1109/TPWRD.2019.2939588.

[8] D. Jovcic, M. Hajian, H. Zhang, and G. Asplund, "Power flow control in DC transmission grids using mechanical and semiconductor based DC/DC devices," in *Proc. 10th IET Int. Conf. AC DC Power Transmiss.*, 2012, pp. 1–6, doi: 10.1049/cp.2012.1972.

[9] Z. Fan, G. Ning, and W. Chen, "Power flow controllers in DC systems," in *Proc. IECON - 43rd Annu. Conf. IEEE Ind. Electron. Soc.*, 2017, pp. 1447–1452, doi: 10.1109/IECON.2017.8216246.

[10] S. Balasubramaniam, C. E. Ugalde-Loo, J. Liang, T. Joseph, R. King, and A. Adamczyk, "Experimental validation of dual H-Bridge current flow controllers for meshed HVdc grids," *IEEE Trans. Power Del.*, vol. 33, no. 1, pp. 381–392, Feb. 2018, doi: 10.1109/TPWRD.2017.2752301.

[11] D. Cheng and J. Zou, "Power flow calculation method of DC grid with interline DC power flow controller (IDCPFC)," in *Proc. IEEE PES Asia-Pacific Power Energy Eng. Conf.*, 2019, pp. 1–5, doi: 10.1109/APPEEC45492.2019.8994677.

[12] W. Chen, X. Zhu, L. Yao, X. Ruan, Z. Wang, and Y. Cao, "An interline DC power-flow controller (IDCPFC) for multiterminal HVDC system," *IEEE Trans. Power Del.*, vol. 30, no. 4, pp. 2027–2036, Aug. 2015, doi: 10.1109/TPWRD.2015.2425412.

[13] J. Sau-Bassols, E. Prieto-Araujo, O. Gomis-Bellmunt, and F. Hassan, "Series interline DC/DC current flow controller for meshed HVDC grids," *IEEE Trans. Power Del.*, vol. 33, no. 2, pp. 881–891, Apr. 2018, doi: 10.1109/TPWRD.2017.2734122.

[14] K. Rouzbehi, J. I. Candela, A. Luna, G. B. Gharehpetian, and P. Rodriguez, "Flexible control of power flow in multiterminal DC grids using DC–DC converter," *IEEE J. Emerg. Sel. Topics Power Electron.*, vol. 4, no. 3, pp. 1135–1144, Sep. 2016, doi: 10.1109/JESTPE.2016.2574458.

[15] J. Liao, Z. Qin, P. Purgat, N. Zhou, Q. Wang, and P. Bauer, "Fault protection and coordinated controls of power flow controller in a flexible DC grid," in *Proc. IEEE 19th Int. Power Electron. Motion Control Conf.*, 2021, pp. 893–898, doi: 10.1109/PEMC48073.2021.9432559.

[16] P. Purgat, L. Mackay, Z. Qin, and P. Bauer, "On the protection of the power flow control converter in meshed low voltage DC networks," in *Proc. IEEE Energy Convers. Congr. Expo.*, Portland, OR, USA, 2018, pp. 478–484.

[17] P. Purgat *et al.*, "Design of a power flow control converter for bipolar meshed LVDC distribution grids," in *Proc. IEEE 18th Int. Power Electron. Motion Control Conf.*, 2018, pp. 1073–1078, doi: 10.1109/EPEPEMC.2018.8521853.

[18] J. Liao, N. Zhou, Y. Huang, and Q. Wang, "Decoupling control for DC electric spring-based unbalanced voltage suppression in a bipolar DC distribution system," *IEEE Trans. Ind. Electron.*, vol. 68, no. 4, pp. 3239–3250, Apr. 2021, doi: 10.1109/TIE.2020.2978714.

[19] J. Liao, N. Zhou, Y. Huang, and Q. Wang, "Unbalanced voltage suppression in a bipolar DC distribution network based on DC electric springs," *IEEE Trans. Smart Grid*, vol. 11, no. 2, pp. 1667–1678, Mar. 2020, doi: 10.1109/TSG.2019.2941874.

[20] F. Wang, Z. Lei, X. Xu, and X. Shu, "Topology deduction and analysis of voltage balancers for DC microgrid," *IEEE J. Emerg. Sel. Topics Power Electron.*, vol. 5, no. 2, pp. 672–680, Jun. 2017, doi: 10.1109/JESTPE.2016.2638959.

[21] G.-H. Gwon, C.-H. Kim, Y.-S. Oh, C.-H. Noh, T.-H. Jung, and J. Han, "Mitigation of voltage unbalance by using static load transfer switch in bipolar low voltage DC distribution system," *Int. J. Elect. Power Energy Syst.*, vol. 90, pp. 158–167, Sep. 2017.

[22] T. Jung, G. Gwon, C. Kim, J. Han, Y. Oh, and C. Noh, "Voltage regulation method for voltage drop compensation and unbalance reduction in bipolar low-voltage DC distribution system," *IEEE Trans. Power Del.*, vol. 33, no. 1, pp. 141–149, Feb. 2018, doi: 10.1109/TPWRD.2017.2694836.

[23] P. Purgat, N. H. van der Blij, Z. Qin, and P. Bauer, "Partially rated power flow control converter modeling for low-voltage DC grids," *IEEE J. Emerg. Sel. Topics Power Electron.*, vol. 8, no. 3, pp. 2430–2444, Sep. 2020, doi: 10.1109/JESTPE.2019.2915166.

[24] J. Liao, N. Zhou, Z. Qin, P. Purgat, Q. Wang, and P. Bauer, "Coordination control of power flow controller and hybrid DC circuit breaker in MVDC distribution networks," *J. Modern Power Syst. Clean Energy*, vol. 9, no. 6, pp. 1257–1268, Nov. 2021, doi: 10.35833/MPCE.2021.000299.

[25] H. Zhang, V. Vittal, G. T. Heydt, and J. Quintero, "A relaxed AC optimal power flow model based on a Taylor series," in *Proc. IEEE Innov. Smart Grid Technol.-Asia*, 2013, pp. 1–5, doi: 10.1109/ISGT-Asia.2013.6698739.

[26] U. Vuyyuru, S. Maiti, and C. Chakraborty, "Active power flow control between DC microgrids," *IEEE Trans. Smart Grid*, vol. 10, no. 5, pp. 5712–5723, Sep. 2019, doi: 10.1109/TSG.2018.2890548.

[27] W. Leterme, P. Tielens, S. De Boeck, and D. Van Hertem, "Overview of grounding and configuration options for meshed HVDC grids," *IEEE Trans. Power Del.*, vol. 29, no. 6, pp. 2467–2475, Dec. 2014, doi: 10.1109/TPWRD.2014.2331106.

Jianquan Liao (Member, IEEE) was born in Fujian, China. He received the B.S degree in electrical engineering from the China University of Petroleum, Qingdao, China, in 2017, and the Ph.D. degree from Chongqing University, Chongqing, China, in 2021. Since 2021, he has been an Associate Research Fellow with the School of Electrical Engineering, Sichuan University, Chengdu, China. From September 2019 to September 2020, he was Guest Researcher of the Delft University of Technology, Delft, The Netherlands. He worked in dc Systems, Energy Conversion and Storage Group in Electrical Sustainable Energy, Delft, The Netherlands. His research interests include power system protection and control, power quality of the dc distribution network, and power system stability and control.

Niancheng Zhou (Member, IEEE) was born in Chongqing, China. He received the B.S., M.S., and Ph.D. degrees from Chongqing University, Chongqing, China, in 1991, 1994, and 1997, respectively. From 1997 to 2003, he was with Chongqing Kuayue Technology Company, Ltd. He is currently a Professor with the School of Electrical Engineering, Chongqing University, China. From 2010 to 2011, he was a Research Fellow of Nanyang Technological University, Singapore. His research interests include the analysis and operation of power systems, microgrids, and power quality.

Zian Qin (Senior Member, IEEE) received the B. Eng. degree in automation from Beihang University, Beijing, China, in 2009, the M.Eng. degree in control science and engineering from the Beijing Institute of Technology, Beijing, China, in 2012, and the Ph.D. degree from Aalborg University, Aalborg, Denmark, in 2015. He is currently an Assistant Professor with the Delft University of Technology, Delft, The Netherlands. In 2014, he was a Visiting Scientist with Aachen University, Aachen, Germany. From 2015 to 2017, he was a Postdoctoral Research Fellow with Aalborg University. His research interests include wide bandgap devices and power-electronics-based grid. He was the Technical Program Chair of IEEE-ISIE 2020, Technical Program Co-Chair of IEEE-COMPEL 2020, and Industrial Session Co-Chair of ECCE-Asia 2020.

Qianggang Wang (Member, IEEE) was born in Fujian, China. He received the B.S. and Ph.D. degrees from Chongqing University, Chongqing, China, in 2009 and 2015, respectively. Since 2015, he has been a Lecturer with the School of Electrical Engineering, Chongqing University. From 2015 to 2016, he was a Research Fellow of Nanyang Technological University, Singapore. His research interests include the analysis and operation of power systems, microgrids, and power quality.

Pavol Bauer (Senior Member, IEEE) received the master's degree in electrical engineering from the Technical University of Kosice, Koğice, Slovakia, in 1985, and the Ph.D. degree from the Delft University of Technology, Delft, The Netherlands, in1995. He is currently a Full Professor with the Department of Electrical Sustainable Energy, Delft University of Technology, and the Head of DC Systems, Energy Conversion and Storage Group, Delft, The Netherlands. He has worked on many projects for industry concerning wind and wave energy, power electronic applications for HVdc systems, projects for smart cities, such as PV charging of electric vehicles, PV and storage integration, and contactless charging. He participated in several Leonardo da Vinci and H2020 EU projects as Project Partner (ELINA, INETELE, E-Pragmatic) and Coordinator (PEMCWebLab. com-Edipe, SustEner, Eranet DCMICRO). He has authored or coauthored more than 72 journal and almost 300 conference papers. His main research interests include protection and control of dc distribution network, power-electronics-based renewable energy system, and electric vehicle.